$CrTe_2$ as a two-dimensional material for topological magnetism in complex heterobilayers

Nihad Abuawwad [1,2,3,*] Manuel dos Santos Dias,[4] Hazem Abusara [3] and Samir Lounis [1,2,†]

[1] *Peter Grünberg Institut and Institute for Advanced Simulation, Forschungszentrum Jülich & JARA, 52425 Jülich, Germany*

[2] *Faculty of Physics, University of Duisburg-Essen and CENIDE, 47053 Duisburg, Germany*

[3] *Department of Physics, Birzeit University, PO Box 14, Birzeit, Palestine*

[4] *Scientific Computing Department, STFC Daresbury Laboratory, Warrington WA4 4AD, United Kingdom*

(Received 30 May 2023; revised 7 August 2023; accepted 23 August 2023; published 5 September 2023)

The discovery of two-dimensional (2D) van der Waals magnetic materials and their heterostructures provided an exciting platform for emerging phenomena with intriguing implications in information technology. Here, based on a multiscale modeling approach that combines first-principles calculations and a Heisenberg model, we demonstrate that interfacing a $CrTe_2$ layer with various Te-based layers enables the control of the magnetic exchange and Dzyaloshinskii-Moriya interactions as well as the magnetic anisotropy energy of the whole heterobilayer, and thereby the emergence of topological magnetic phases such as skyrmions and antiferromagnetic Néel merons. The latter are novel particles in the world of topological magnetism since they arise in a frustrated Néel magnetic environment and manifest as multiples of intertwined hexamer textures. Our findings pave a promising road for proximity-induced engineering of both ferromagnetic and long-sought antiferromagnetic chiral objects in the very same 2D material, which is appealing for information technology devices employing quantum materials.

DOI: 10.1103/PhysRevB.108.094409

I. INTRODUCTION

Since the experimental demonstration of two-dimensional (2D) van der Waals (vdWs) magnets with intrinsic magnetism in 2017 [1,2], research interest in 2D magnetic nanomaterials has grown rapidly due to their potential applications in spintronic devices and their significance in fundamental physical studies [3–10]. The possibility of heterostructuring offers the unprecedented possibility to engineer quantum materials with exquisite properties facilitated by the quasiperfect interfaces expected by the vdW gaps. This enables the realization of heterostructures hosting functionalities that are not otherwise seen in the individual building blocks. In most cases, these 2D materials have a simple collinear magnetic order, such as ferromagnetic or antiferromagnetic. However, they can also exhibit complex noncollinear magnetism and host ferromagnetic skyrmions, to give just two examples [11–13]. Skyrmions are topologically-protected chiral spin textures of great interest for potential applications as information carriers in information technology devices [14–16]. These chiral magnetic states typically arise due to the interplay between Heisenberg exchange and relativistic Dzyaloshinskii-Moriya interaction (DMI) [17,18] in materials that lack inversion symmetry and have nonzero spin-orbit coupling. In a 2D material, skyrmions arise when the magnetization points out of the plane of the magnetic layer. When the magnetization is in-plane it instead gives rise to merons, which represent another form of chiral spin textures. The topological charge for skyrmions is integer, while it it half-integer for merons, hence both kinds of spin textures are qualitatively distinct [19–21].

In the context of 2D heterostructures, ferromagnetic (FM) Néel-type skyrmions were experimentally detected in Fe_3GeTe_2 [22–26], while FM merons were only evidenced in thin films and disks [27–30]. Theoretically, a free-standing monolayer of $CrCl_3$ has been predicted to host such half-integer spin textures, which are stabilized by the magnetic dipolar coupling that favors an overall in-plane orientation of the magnetization [31]. Another 2D material, which is attracting interest due to its high magnetic ordering temperature is $CrTe_2$. Recent studies have shown that a thin $CrTe_2$ layer grown either on SiO_2/Si or heterobilayer graphene substrates is ferromagnetic with a high Curie temperature of 200 K [32,33]. In contrast, a different study on a single monolayer of $CrTe_2$ deposited on graphene indicated a zigzag antiferromagnetic ground state while a magnetic field drives a transition to a noncollinear spin texture [34]. We found that it exhibits magnetic frustration and strong magnetoelastic coupling, which depending on the resulting magnetic state leads to breaking of inversion symmetry and the emergence of DMI [35]. However, no magnetic skyrmions have been found in this material.

Here, we explore the possibility of engineering 2D topological magnetism in a $CrTe_2$ monolayer by constructing heterostructures with Te-based layers involving other nonmagnetic transition metal atoms (see Fig. 1). Utilizing a multipronged approach based on first-principles calculations combined with an extended Heisenberg model, we unveil here topological antiferromagnetic (AFM) objects already arising in the free-standing 1T phase of $CrTe_2$. These objects consist of multimeronic particles emerging in a frustrated in-plane Néel magnetic environment. Such AFM topological states have long been sought in the context of skyrmionics as ideal information carriers, since they are expected to be unaffected

*Corresponding author: n.abuawwad@fz-juelich.de

†Corresponding author: s.lounis@fz-juelich.de

(a)

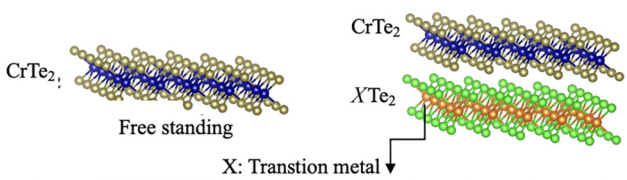

Ti	V	Cr	Mn	Fe	Co	Ni	Cu	Zn
Zr	Nb	Mo	Tc	Ru	Rh	Pd	Ag	Cd
Hf	Ta	W	Re	Os	Ir	Pt	Au	Hg

Red: nonmagnetic XTe_2 monolayers (lattice mismatching < 3%).
Blue: nonmagnetic XTe_2 monolayers (lattice mismatching >4%).
Green: magnetic XTe_2 monolayers (lattice mismatching <3%, except Fe = 4.2 %)

(b)

Structure	Metastable state
Free standing, $CrTe_2$/(Ti, Nb, Ta) Te_2	AFM-merons
$CrTe_2$/(Zr, Ni, Rh) Te_2	FM-Skyrmions

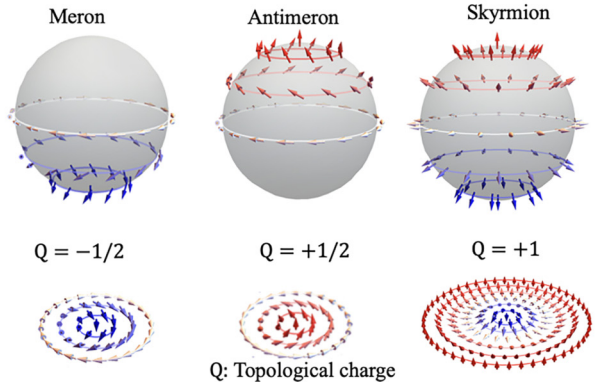

FIG. 1. Overview of the heterostructures and magnetic states. (a) $CrTe_2/XTe_2$ heterobilayer, where X is the transition metal from the table and we chose to study those highlighted in red. (b) Table listing the topological magnetic states found in the $CrTe_2/XTe_2$ heterobilayer, with X being the transition metal in red color. The spin textures of a meron, antimeron, and skyrmion are illustrated together with the stereographic projection to a sphere, which visually corresponds to the different topological charges.

by the skyrmion Hall effect [15,36–41] responsible for the undesired deflection of conventional skyrmions from a straight trajectory upon application of a current. Their AFM nature should also lead to a weak sensitivity to external magnetic fields and potentially terahertz dynamics [42,43], further motivating efforts towards their experimental realization. Once interfaced with various Te-based layers containing either heavy or light transition metal atoms, we demonstrate the ability to engineer the stability and nature of the underlying magnetic state. Surprisingly, with the right vdW heterostructure, the AFM merons can be converted to FM skyrmions, which opens unique opportunities for designing devices made of 2D materials to realize fundamental concepts for information technology based on topological magnetic bits.

II. METHODS

A. First-principles calculations

Structural relaxations of $CrTe_2/XTe_2$ heterobilayer were assessed using density functional theory (DFT) as implemented in the Quantum Espresso (QE) computational package [44] with projector augmented plane-wave (PAW) pseudopotentials [45]. In our calculations, the generalized gradient approximation (GGA) of Perdew-Burke-Ernzerhof (PBE) [46] was used as the exchange and correlation functional. The plane-wave energy cut-off is 80 Ry, and the convergence criterion for the total energy is set to 0.01 μRy. The self-consistent calculations were performed with a k mesh of $24 \times 24 \times 1$ points and the Brillouin zone summations used a Gaussian smearing of 0.01 Ry. We included a vacuum region of 30 Å in the direction normal to the plane of the heterobilayer to minimize the interaction between the periodic images. The unit-cell parameters and the atomic positions were optimized by ensuring that the residual forces on the relaxed atomic positions were smaller than 1mRy a_0^{-1} and the pressure on the unit cell smaller than 0.5 kbar.

Once the geometries of the various collinear magnetic states were established, we explored in detail magnetic properties and interactions with the all-electron full-potential relativistic Korringa-Kohn-Rostoker Green's function (KKR-GF) method as implemented in the JuKKR computational package [47–49]. The angular momentum expansion of the Green's function was truncated at $\ell_{\max} = 3$ with a k mesh of $48 \times 48 \times 1$ points. The energy integrations were performed including a Fermi-Dirac smearing of 502.78 K, and the local spin-density approximation was employed [50]. The Heisenberg exchange interactions and Dzyaloshinskii-Moriya (DM) vectors were extracted using the infinitesimal rotation method [51] with a finer k mesh of $200 \times 200 \times 1$.

B. Magnetic interactions and atomistic spin dynamics

The magnetic interactions obtained from the first-principles calculations are used to parametrize the following classical extended Heisenberg Hamiltonian with unit spins, $|\mathbf{S}| = 1$, which includes the Heisenberg exchange coupling (J), the DMI (D), the magnetic anisotropy energy (K), and the Zeeman term (B),

$$E = -\sum_i \mathbf{B}\cdot\mathbf{S}_i - \sum_i K_i\left(S_i^z\right)^2 - \sum_{i,j} J_{ij}\mathbf{S}_i\cdot\mathbf{S}_j - \sum_{i,j}\mathbf{D}_{ij}\cdot(\mathbf{S}_i\times\mathbf{S}_j). \quad (1)$$

Here i and j label different magnetic sites within a unit cell. The calculated magnetic interactions are long ranged and display an oscillatory behavior as function of distance, as expected on metals, which can lead to energetic competition between different magnetic states and to the stabilization of magnetic spirals. Numerically, we found that the identified ground state is robust once interactions up to a distance of six times the nearest-neighbor distance are incorporated in the simulations. Taking the free-standing case as an example, if we include only the interactions up to the fourth nearest-neighbor distance we find that the ground state is the noncollinear Néel-AFM state, while taking more interactions into account transforms the ground state into a spin-spiral state. The magnetic properties pertaining to $CrTe_2$ were evaluated by analyzing the Fourier-transformed magnetic interactions, which in reciprocal space gives access to

the magnetic ground state and the related dispersion of potential spin spirals: $J_{ij}(\mathbf{q}) = \sum_j J_{0j} e^{-i\mathbf{q}\cdot\mathbf{R}_j}$, where $\mathbf{R}_{0j}$ is a vector connecting unit cells atom 0 and j.

Furthermore, atomistic spin dynamic simulations using the Landau-Lifshitz equation (LLG) as implemented in the Spirit code [52,53] are performed in order to explore potential complex magnetic states while the geodesic nudged elastic band (GNEB) is utilized for investigating if these magnetic states are metastable [43,52,54,55]. We used the simulated annealing method: we started from a random spin state at 1000 K, which we let equilibrate, then cool the system in steps by reducing the temperature to half of its previous value and equilibrating again, until we reach below 10 K. The value of the Gilbert damping rate in our simulation was set to 0.1. We considered the 2D hexagonal lattice defined by the Cr atoms, with a cell size of 100 × 100 with periodic boundary conditions.

III. RESULTS AND DISCUSSION

A. Topological AFM state in monolayer $CrTe_2$

The 1T phase of free-standing $CrTe_2$ monolayer is characterized by a magnetic moment of 2.67 μ_B. The magnetic interactions favor antiferromagnetism, which on a triangular lattice usually leads to the Néel phase in which neighboring magnetic moments have an angle of 120°. It can be partitioned into three FM sublattices named α, β, and γ as shown in Fig. 2(b). The Heisenberg exchange interactions are illustrated graphically in terms of distance as depicted in Fig. 5(g) below. The value of $J_1 = -5.36$ and $J_2 = 4.01$ meV would lead to a Néel ground state, but the interactions are long ranged and introduce competing tendencies, resulting in a frustrated spin-spiraling state with an energy minimum close to the Néel state [Fig. 2(a)]. This spin spiral is further modified by the magnetic anisotropy (1.4 meV), which favors an in-plane orientation for the magnetic moment, and finally leads to the discovery of a topological AFM state made of a hexamer of meronic texture.

In order to understand the origin of this magnetic phase, we show in Fig. 2(c) that the topological AFM state arises from various combinations of meronic textures coexisting as pairs (meron-meron, meron-antimeron, and antimeron-antimeron) in each of the three AFM sublattices. We note that within each sublattice, these pairs are ferromagnetic. The topological charge (t) for a meron is determined by the product $pw/2$, where w is the winding number w, which describes the in-plane rotation of the magnetic moments with $w = +1$ (–1) for vortex (antivortex). The polarity p describes the out-of-plane core magnetization ($p = +1$ for up, and $p = -1$ for down). This leads to a value of $t = -1/2$ ($t = +1/2$) for a meron (antimeron). Various combinations of meronic states can emerge, leading to a rich set of the possible values of the total topological charge T illustrated in Fig. 2(d). The first scenario illustrated in Fig. 2(c) corresponds to a meronic hexamer with zero total topological charge ($T = 0$), which can arise either when each sublattice accommodates a meron-antimeron pair ($t = 0$), or when hosting pairs of meron-meron pair ($t = 1$), antimeron-antimeron ($t = -1$), and meron-antimeron ($t = 0$). The second and third scenarios have an opposite total topological charge of +1 and −1. The state with $T = 1$ (−1) occurs either when two sublattices have meron-antimeron pairs carrying a charge $t = 0$ and third sublattice contains an antimeron-antimeron pair of a charge $t = 1$ (meron-meron pair with $t = -1$), or when two sublattices have antimeron-antimeron pairs with $t = 1$ (meron-meron pairs with $t = -1$) while the remaining sublattice host a meron-meron pair of charge $t = -1$ (antimeron-antimeron with $t = 1$).

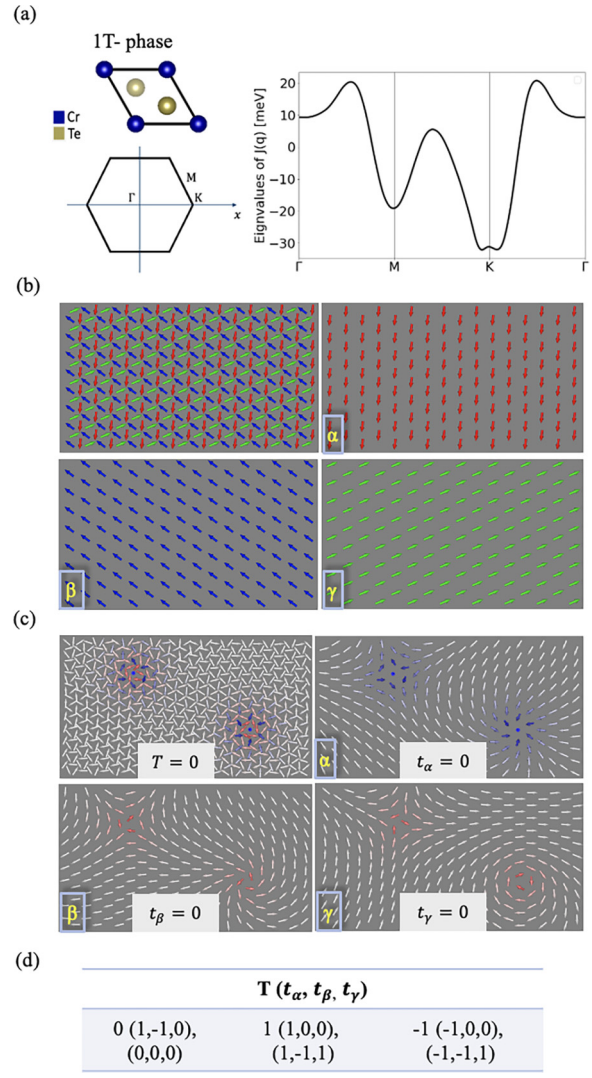

FIG. 2. (a) The unit cell utilized for the simulation of the 1T phase of the free-standing monolayer of $CrTe_2$ (top), the hexagonal first Brillouin zone (bottom), and eigenvalues of the Fourier-transformed exchange interactions as a function of q in in free standing of $CrTe_2$ (right). (b) Decomposition of the Néel state into three ferromagnetic sublattices α, β, and γ carrying moments rotated by 120°. (c) Frustrated AFM multimeronic spin textures. The total topological charge Q is decomposed into the three sublattices, each of which hosts a pair of merons with sublattice-dependent topological charges t_i ($i = \alpha, \beta, \gamma$). Here the magnetic background is the spin-spiraling ground state, which is very close to the Néel state. (d) Total topological charge T and how it arises from various possible combinations of the topological charges from each sublattice.

Having established the existence of AFM meronic objects, we investigate if they are metastable by utilizing a series of geodesic nudged elastic band (GNEB) simulations. Figure 3(a) displays the minimum energy path for the collapse

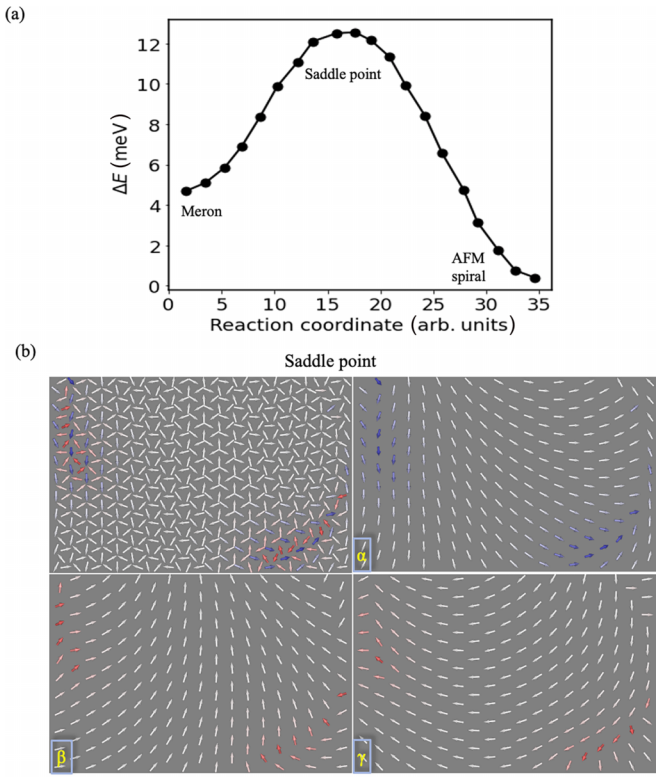

FIG. 3. (a) Energy path for the collapse of the single pair of the AFM meronic state hosted by the free-standing $CrTe_2$ layer. The spin texture associated with the saddle point is illustrated in (b).

of the topological AFM state, which hosts an energy barrier of 7.9 meV [more details on the saddle point are shown in Fig. 3(b)].

B. Topological magnetic states in $CrTe_2/XTe_2$ heterobilayers

Motivated by the intriguing magnetic behavior of the single $CrTe_2$ layer, we explore proximity-induced magnetic phases upon interfacing with various XTe_2 monolayers, X being a transition metal atom. Our systematic structural investigation of the different junctions enabled us to categorize them into three groups, as illustrated in Fig. 1(a): The first group hosts nonmagnetic XTe_2 layers with a small lattice mismatch (less than 3%) with $CrTe_2$ such as (Zr, Nb, Rh, Ni, Ti)Te_2, and this is the group that we focus in our study. The second and third groups were disregarded since they have either a large lattice mismatch (more than 4%) or are magnetic, which would lead to more complex proximity-induced effects to be explored in future studies.

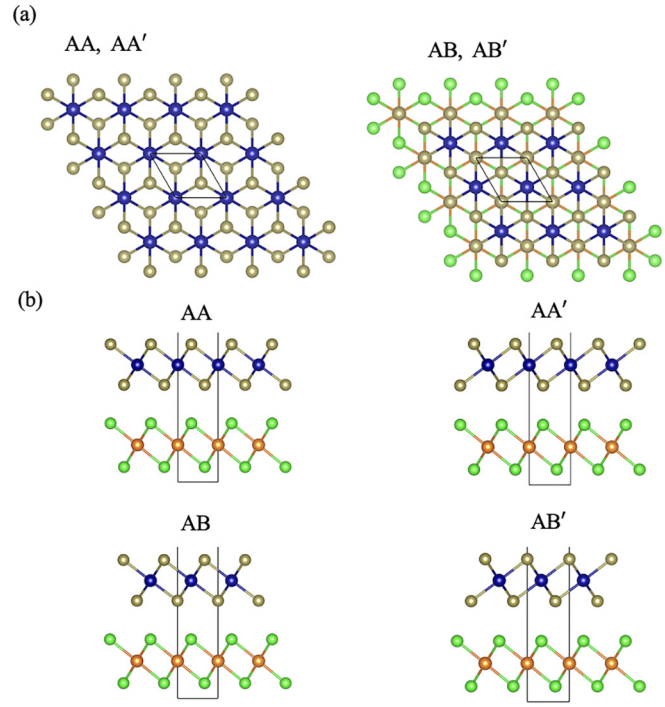

FIG. 4. The different AA, AA′, AB, and AB′ stacking arrangements for $CrTe_2/XTe_2$ heterobilayers. (a) Top and (b) side views.

The heterobilayers made of $CrTe_2$ and nonmagnetic XTe_2 were built assuming four different stacking (AA, AA′, AB, and AB′) as illustrated in Fig. 4. In the AA stacking, which is the ground state (see Table I), Cr is vertically aligned with the transition metal X, and the Te layers forming the interface are shifted with respect to each other, while in the AA′ arrangement they are stacked on top of each other. In the AB and AB′ structures Cr and X are no longer vertically aligned, and the two structures are distinguished by the stacking arrangement of the Te layers at the interface. In the following we focus our investigation on the AA stacking.

Table II shows the lattice parameters, including lattice constant and interlayer distance, for the AA stacking order. It is clear that these parameters vary significantly depending on the transition metal in the Te-based layers. The lattice constants can be grouped around two values: ∼3.7 Å for $CrTe_2$/(Ti, Nb, Ta)Te_2 heterobilayer, which is close to the lattice constant of the free-standing CrTe2 monolayer, and ∼3.8 Å in $CrTe_2$/(Zr, Ni, Rh)Te_2 heterobilayer, which is similar to the value of the bulk $CrTe_2$ lattice constant and results from the strain created at the interface.

TABLE I. Total energy difference between various stacking orders and the ground-state AA structure for all $CrTe_2/XTe_2$ heterobilayers. Energies in meV.

	$CrTe_2$ on top of					
Stacking	$TiTe_2$	$NbTe_2$	$TaTe_2$	$NiTe_2$	$ZrTe_2$	$RhTe_2$
AA′	105.3	126.9	125.9	149.1	130.1	185.5
AB	30.3	27.3	26.4	103.6	60.5	120.8
AB′	9.9	4.6	8.2	4.8	23.7	61.6

TABLE II. Lattice constant a, interlayer distance h, magnetic anisotropy energies K, and Dzyaloshinskii-Moriya interaction D of the $CrTe_2/XTe_2$ heterobilayers in the AA stacking. As a reference the free-standing $CrTe_2$ has a lattice constant of 3.71 Å with a magnetic anisotropy of 1.40 meV and zero DMI.

	$CrTe_2$ on top of					
	$TiTe_2$	$NbTe_2$	$TaTe_2$	$NiTe_2$	$ZrTe_2$	$RhTe_2$
a (Å)	3.73	3.70	3.70	3.81	3.82	3.79
h (Å)	3.76	3.65	3.74	3.46	3.75	3.50
K (meV)	0.95	0.90	0.94	0.90	0.61	1.70
$\lvert\mathbf{D}_1\rvert$ (meV)	0.21	0.23	0.27	0.30	0.30	0.45
D_1^z (meV)	0.10	0.15	0.22	0.05	0.06	0.06
$\lvert\mathbf{D}_2\rvert$ (meV)	0.48	0.37	0.48	0.60	0.61	0.71
D_2^z (meV)	0.15	0.18	0.20	0.01	0.01	0.12
$\lvert\mathbf{D}_3\rvert$ (meV)	0.38	0.27	0.30	0.31	0.32	0.35
D_3^z (meV)	0.05	0.05	0.05	0.02	0.02	0.80

Now we turn to the analysis of the magnetic properties of all heterobilayers in the AA stacking. In the first scenario, where the interfacing Te-based layer contains Ta, Nb, or Ti, the Heisenberg exchange interactions induce a frustrated spin-spiraling state with an energy minimum close to the Néel state [Figs. 5(a) and 5(g)], where J_1 possesses the most negative value in the heaviest Te-based layer ($TaTe_2$), while J_2 holds the most positive value in the less lightest Te-based layer ($TiTe_2$). Once interactions induced by the spin-orbit interaction included, AFM multimeronic spin textures emerge similar to the free-standing case [Fig. 5(b)]. Adding the substrate layer breaks the inversion symmetry of the $CrTe_2$ monolayer and introduces the DMI, where the z component of the of the DM vector for the first- and second-nearest neighbors favors in-plane rotations of the magnetic moments and so is compatible with the underlying in-plane magnetic anisotropy (Table II). This enhances the stability of the AFM topological objects, as can be identified by the increased energy barrier illustrated in Fig. 5(c). Therefore, the heterobilayer with the largest z component of the DMI has the highest energy barrier. The energy barrier for the bilayers with $TiTe_2$, $NbTe_2$, and $TaTe_2$ is 0.2 meV, 0.4 meV, and 2.2 meV higher than the one for free-standing $CrTe_2$, respectively, and the increased stability correlates with the increase in the magnitude of the DM interaction going from Ti to Nb to Ta, as listed in Table II. We note that the MAE is roughly constant for all investigated interfaces (∼0.9 meV). Interestingly, the radius r of each of the merons and the distance d between the them [illustrated in Fig. 5(b)] show opposite trends. The radius increases for the heterobilayers, with values of 2.6 nm ($TiTe_2$), 2.7 nm ($NbTe_2$), and 2.8 nm ($TaTe_2$) larger than the one for the free-standing $CrTe_2$ (2.4 nm), and follows the increase of the out-of-plane DMI. Conversely, the distance between the two merons is progressively reduced: $d = 34.8$ nm for free-standing $CrTe_2$ and 34.4, 34.3, and 34.0 nm once it is interfaced with $TiTe_2$, $NbTe_2$, and $TaTe_2$, respectively. We verified that the relation between the distance between merons and their size is independent from the size of the simulation box.

In the second scenario, $CrTe_2$ is interfaced with Te-based layers hosting either Zr, Ni, or Rh. As mentioned before, these layers impose a lattice strain on $CrTe_2$ that switches the magnetic ground state from AFM to FM based on the Heisenberg exchange interactions [see energy minimum in Fig. 5(d), and the values of Heisenberg exchange interactions in Fig. 5(h); one can see that the J's have a positive value up to four-nearest neighbor with $J_1 = 2$ meV in the three heterobilayers]. Once DMI and MAE are taken into account (see values in Table II), Néel-type skyrmionic domains form in zero magnetic field as shown in Fig. 5(e). For the calculation of energy barriers we select isolated skyrmions, resulting in the spin texture shown in Fig. 6(d), revealing that they are metastable. A magnetic field larger than 6 T transforms the skyrmionic domain state to a triangular lattice of skyrmions, Fig. 5(f), which is more stable than the FM state by 3.1, 2.8, and 2.2 meV for the Rh, Ni, and Zr-based heterobilayers, respectively. Next we explore if an isolated skyrmion in a FM background is metastable, for which GNEB simulations led to the energy barriers plotted in Fig. 6(b). The barrier that has to be overcome to allow the skyrmion to relax to the FM state increases going from Ni (6 meV) to Zr (7 meV) to the Rh-based bilayer (8 meV), which decreases with increasing the magnetic field as shown in Fig. 6(d) [56,57]. In this case the MAE depends more strongly on the nature of the heterobilayer (e.g., it is almost twice as large for Rh than for Ni), and hence has a stronger influence on the energy barrier and also on the skyrmion radius. A larger energy difference between the skyrmion and the FM state corresponds to a larger skyrmion radius, and as expected they all shrink in size when the magnitude of the applied magnetic field is increased [Fig. 6(c)], disappearing above about 30 T. In contrast, applying an external magnetic field to the AFM merons found for the Ti, Nb, and Ta-based heterobilayers has no noticeable effect on their radius, but the underlying total topological charge changes at approximately 12 T from ±1 to 0 (see Table III for more details).

IV. CONCLUSIONS

In summary, we demonstrated that the monolayer of $CrTe_2$ in the 1T phase can host various topological magnetic states once interfaced with nonmagnetic Te-based layers hosting transition metals by using a combination of density functional theory calculations and atomistic spin dynamics. The scrutinized quantum materials were preselected to be within an acceptable range of lattice mismatching, which makes the

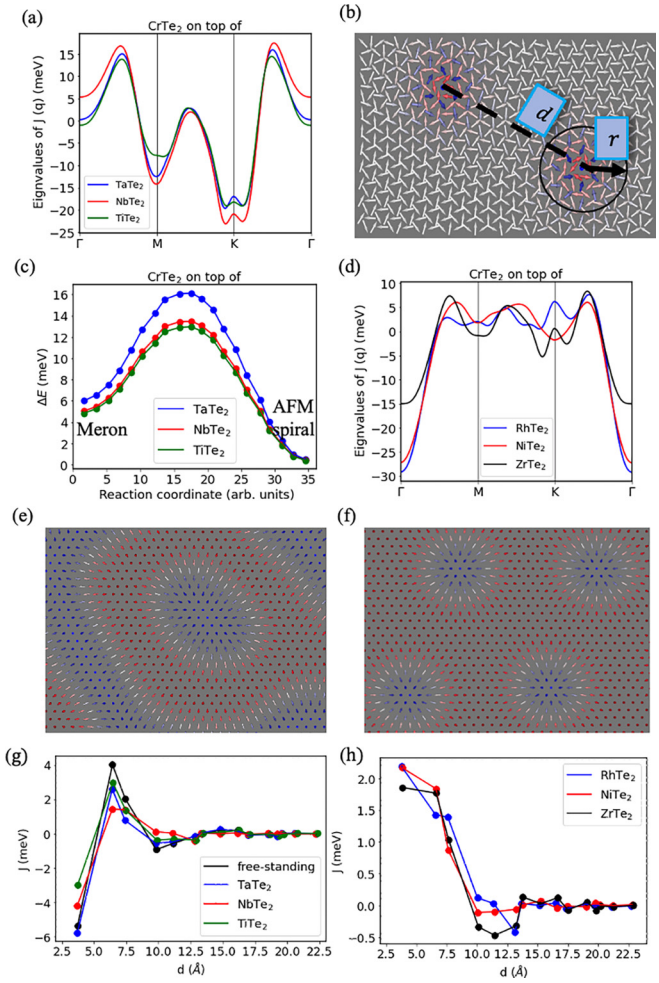

FIG. 5. Topological magnetic textures in heterobilayers. In (a)–(c), (g) and (d)–(f), (h) results related respectively to $CrTe_2$/(Ti,Nb,Ta)Te_2 and $CrTe_2$/(Zr, Ni, Rh)Te_2 heterobilayers. [(a),(d)] Eigenvalues of the Fourier-transformed exchange interactions as a function of q. (b) An example of an AFM meronic texture indicating the radius r of each meron and the distance d between the meronic partners. (c) Energy path for the collapse of a single pair of AFM merons in the heterobilayers. (e) Zero-field skyrmionic-like magnetic state in the heterobilayers. (f) Skyrmionic lattice formed upon application of a magnetic field of 6 T. [(g),(h)] The Heisenberg exchange interactions as a function of distance d, where d is a function of lattice constant.

considered atomic structures realistic and hence make our predictions of the magnetic properties more reliable.

Our main finding is the emergence of a type of antiferromagnetic topological state consisting of hexamer-meronic spin texture in a magnetically frustrated environment characterizing the free-standing $CrTe_2$ as well as the $CrTe_2$/(Ta, Nb, Ti)Te_2 heterobilayers. This magnetic state forms in a rich set of pair combinations of merons and antimerons, with each pair living in one of the three antiferromagnetic sublattices. By constructing the vdW bilayers, inversion symmetry is broken, which gives rise to a z component of the Dzyaloshinskii-Moriya interaction that enhances the stability of these meronic textures.

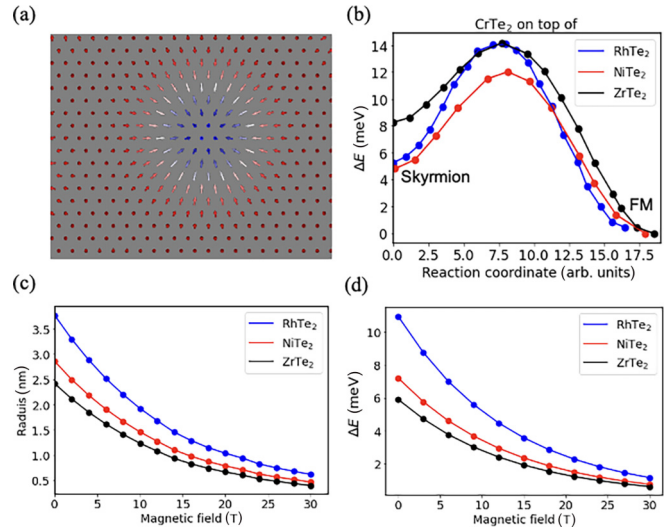

FIG. 6. Single skyrmion in $CrTe_2$/(Zr, Ni, Rh)Te_2 heterobilayers. (a) Single skyrmion selected to calculate energy barriers and explore its stability. (b) Energy path for the collapse of the single skyrmion. (c) The radius of a single skyrmion and energy barriers, obtained with GNEB simulations, as a function of magnetic field.

Intriguingly, when $CrTe_2$ is instead proximitized with (Zr, Rh, Ni)Te_2 layers it displays ferromagnetic behavior, which is imposed by the interface-induced strain, hosting spin spirals as well as ferromagnetic skyrmions, which are both enabled by the DMI. These results provide a potential explanation for the anomalous Hall effect identified in the $CrTe_2$/$ZrTe_2$ heterostructures [58]. We note that a recent paper predicts the formation of skyrmions in $CrTe_2$/WTe_2 bilayer [59], which is an interface that we disregarded because of the large lattice mismatch.

Overall, our paper highlights $CrTe_2$ as a promising 2D layer for further exploration of proximity-induced topological magnetism enabled by its strong magneto-elastic coupling [35]. Our findings suggest the possibility of engineering the size and stability of the underlying topological spin textures by modifying the nature of the interfacing 2D material. More importantly, we anticipate that besides the fundamental importance of identifying the frustrated antiferromagnetic multimeronic textures, patching the same 2D material such as $CrTe_2$ with distinct 2D layers such as those unveiled in this paper, favoring either ferromagnetic skyrmions of antiferromagnetic merons, can be useful constituents of information

TABLE III. Effect of the magnetic field on the topological charge of the AFM multimeronic spin texture. Shown are the total topological charge T and how it arises from the contributions of the individual sublattices t_i.

Topological charges T $(t_\alpha, t_\beta, t_\gamma)$	
$B = 0$ T	$B = 12$ T
0 (0, 0, 0), (0, –1, 1)	0 (0, 0, 0), (0, –1, 1)
1 (1, 0, 0), (1, –1, 1)	0 (0, 0, 0), (0, –1, 1)
–1 (–1, 0, 0), (–1, –1, 1)	0 (0, 0, 0), (0, –1, 1)

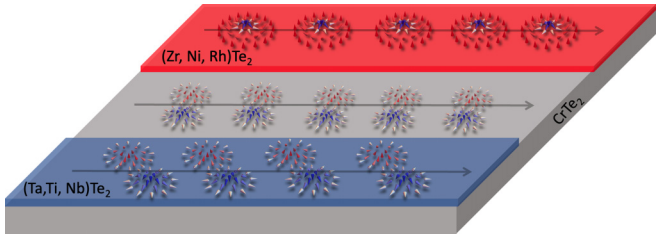

FIG. 7. Potential technological device concept combining 2D $CrTe_2$ with other 2D layers, such as (Ta, Nb, Ti)Te_2, which promote antiferromagnetic merons as topological magnetic defects, and (Zr, Rh, Ni)Te_2 layers that promote ferromagnetic skyrmions. The various types of topological spin textures can then be injected from one device region to another, and driven using applied spin currents or thermal gradients, for instance.

technology devices. We envisage, for instance, their potential application for the ultimate control and transport of dissimilar topological objects to carry information in well-designed regions of multiple 2D vdW heterojunctions, as schematically depicted in Fig. 7. By having both FM skyrmions and AFM merons in the same device, it becomes possible to harness their unique characteristics for different functionalities. Skyrmions could be used for data storage and transmission, while merons might be employed for logic operations and signal processing. This allows for a single device to perform multiple tasks efficiently, leading to more compact and versatile spintronic systems. Moreover, coexistence of skyrmions and merons can be utilized in hybrid memory devices, involving both FM and AFM topological solitons, where one type of spin texture complements the other. For example, skyrmions might serve as nonvolatile memory elements for data storage, while merons could act as intermediate states during data processing and manipulation.

ACKNOWLEDGMENTS

We acknowledge fruitful discussions with Amal Aldarawsheh, Jose Martinez-Castro, and Markus Ternes. This work was supported by the Federal Ministry of Education and Research of Germany in the framework of the Palestinian-German Science Bridge (BMBF Grant No. 01DH16027). We acknowledge funding provided by the Priority Programmes SPP 2244 "2D Materials Physics of van der Waals heterobilayer" (Project LO 1659/7-1) and SPP 2137 Skyrmionics (Projects LO 1659/8-1) of the Deutsche Forschungsgemeinschaft (DFG). We acknowledge the computing time granted by the JARA-HPC Vergabegremium and VSR commission on the supercomputer JURECA at Forschungszentrum Jülich [60]. The work of MdSD made use of computational support by CoSeC, the Computational Science Centre for Research Communities, through CCP9.

[1] B. Huang, G. Clark, E. Navarro-Moratalla, D. R. Klein, R. Cheng, K. L. Seyler, D. Zhong, E. Schmidgall, M. A. McGuire, D. H. Cobden *et al.*, Nature (London) **546**, 270 (2017).
[2] C. Gong, L. Li, Z. Li, H. Ji, A. Stern, Y. Xia, T. Cao, W. Bao, C. Wang, Y. Wang *et al.*, Nature (London) **546**, 265 (2017).
[3] M. Gibertini, M. Koperski, A. F. Morpurgo, and K. S. Novoselov, Nat. Nanotechnol. **14**, 408 (2019).
[4] C. Gong and X. Zhang, Science **363**, eaav4450 (2019).
[5] M. A. McGuire, J. Appl. Phys. **128**, 110901 (2020).
[6] X. Jiang, Q. Liu, J. Xing, N. Liu, Y. Guo, Z. Liu, and J. Zhao, Appl. Phys. Rev. **8**, 031305 (2021).
[7] J. F. Sierra, J. Fabian, R. K. Kawakami, S. Roche, and S. O. Valenzuela, Nat. Nanotechnol. **16**, 856 (2021).
[8] S. Rahman, J. F. Torres, A. R. Khan, and Y. Lu, ACS Nano **15**, 17175 (2021).
[9] K. S. Burch, D. Mandrus, and J.-G. Park, Nature (London) **563**, 47 (2018).
[10] H. Li, S. Ruan, and Y.-J. Zeng, Adv. Mater. **31**, 1900065 (2019).
[11] A. Edström, D. Amoroso, S. Picozzi, P. Barone, and M. Stengel, Phys. Rev. Lett. **128**, 177202 (2022).
[12] D. Amoroso, P. Barone, and S. Picozzi, Nat. Commun. **11**, 5784 (2020).
[13] G. Qiu, Z. Li, K. Zhou, and Y. Cai, npj Quantum Mater. **8**, 15 (2023).
[14] A. N. Bogdanov and C. Panagopoulos, Nat. Rev. Phys. **2**, 492 (2020).
[15] N. Nagaosa and Y. Tokura, Nat. Nanotechnol. **8**, 899 (2013).
[16] A. Fert, N. Reyren, and V. Cros, Nat. Nanotechnol. **2**, 899 (2013).
[17] T. Moriya, Phys. Rev. **120**, 91 (1960).
[18] J. Phys. Chem. Solids **4**, 241 (1958).
[19] B. Göbel, I. Mertig, and O. A. Tretiakov, Phys. Rep. **895**, 1 (2021).
[20] H. Jani, J.-C. Lin, J. Chen, J. Harrison, F. Maccherozzi, J. Schad, S. Prakash, C.-B. Eom, A. Ariando, T. Venkatesan, and P. G. Radaelli, Nature (London) **590**, 74 (2021).
[21] X. Li, L. Shen, Y. Bai, J. Wang, X. Zhang, J. Xia, M. Ezawa, O. A. Tretiakov, X. Xu, M. Mruczkiewicz *et al.*, npj Comput. Mater. **6**, 169 (2020).
[22] Y. Wu, S. Zhang, J. Zhang, W. Wang, Y. L. Zhu, J. Hu, G. Yin, K. Wong, C. Fang, C. Wan *et al.*, Nat. Commun. **11**, 3860 (2020).
[23] M. T. Birch, L. Powalla, S. Wintz, O. Hovorka, K. Litzius, J. C. Loudon, L. A. Turnbull, V. Nehruji, K. Son, C. Bubeck *et al.*, Nat. Commun. **13**, 3035 (2022).
[24] A. Chakraborty, A. K. Srivastava, A. K. Sharma, A. K. Gopi, K. Mohseni, A. Ernst, H. Deniz, B. K. Hazra, S. Das, P. Sessi *et al.*, Adv. Mater. **34**, 2108637 (2022).
[25] Y. Wu, B. Francisco, Z. Chen, W. Wang, Y. Zhang, C. Wan, X. Han, H. Chi, Y. Hou, A. Lodesani *et al.*, Adv. Mater. **34**, 2110583 (2022).
[26] T.-E. Park, L. Peng, J. Liang, A. Hallal, F. S. Yasin, X. Zhang, K. M. Song, S. J. Kim, K. Kim, M. Weigand, G. Schütz, S. Finizio, J. Raabe, K. Garcia, J. Xia, Y. Zhou, M. Ezawa, X. Liu, J. Chang, H. C. Koo *et al.*, and Phys. Rev. B **103**, 104410 (2021).
[27] X. Fu, S. D. Pollard, B. Chen, B.-K. Yoo, H. Yang, and Y. Zhu, Sci. Adv. **4**, eaat3077 (2018).

[28] N. Gao, S. G. Je, M. Y. Im, J. W. Choi, M. Yang, Q. Li, T. Y. Wang, S. Lee, H. S. Han, K. S. Lee *et al.*, Nat. Commun. **10**, 5603 (2019).
[29] F. P. Chmiel, N. W. Price, R. D. Johnson, A. D. Lamirand, J. Schad, G. van der Laan, D. T. Harris, J. Irwin, M. S. Rzchowski, C. B. Eom, and P. G. Radaelli, Nat. Mater. **17**, 581 (2018).
[30] C. Phatak, A. K. Petford-Long, and O. Heinonen, Phys. Rev. Lett. **108**, 067205 (2012).
[31] X. Lu, R. Fei, L. Zhu, and L. Yang, Nat. Commun. **11**, 4724 (2020).
[32] L. Meng, Z. Zhou, M. Xu, S. Yang, K. Si, L. Liu, X. Wang, H. Jiang, B. Li, P. Qin *et al.*, Nat. Commun. **12**, 809 (2021).
[33] X. Zhang, Q. Lu, W. Liu, W. Niu, J. Sun, J. Cook, M. Vaninger, P. F. Miceli, D. J. Singh, S.-W. Lian *et al.*, Nat. Commun. **12**, 2492 (2021).
[34] J.-J. Xian, C. Wang, J.-H. Nie, R. Li, M. Han, J. Lin, W.-H. Zhang, Z.-Y. Liu, Z.-M. Zhang, M.-P. Miao *et al.*, Nat. Commun. **13**, 257 (2022).
[35] N. Abuawwad, M. Dos santos Dias, H. Abusara, and S. Lounis, J. Phys.: Condens. Matter **34**, 454001 (2022).
[36] X. Zhang, Y. Zhou, and M. Ezawa, Sci. Rep. **6**, 24795 (2016).
[37] J. Barker and O. A. Tretiakov, Phys. Rev. Lett. **116**, 147203 (2016).
[38] Y. Hirata, D.-H. Kim, S. K. Kim, D.-K. Lee, S.-H. Oh, D.-Y. Kim, T. Nishimura, T. Okuno, Y. Futakawa, H. Yoshikawa *et al.*, Nat. Nanotechnol. **14**, 232 (2019).
[39] A. Aldarawsheh, I. L. Fernandes, S. Brinker, M. Sallermann, M. Abusaa, S. Blügel, and S. Lounis, Nat. Commun. **13**, 7369 (2022).
[40] W. Jiang, X. Zhang, G. Yu, W. Zhang, X. Wang, M. B. Jungfleisch, J. E. Pearson, X. Cheng, O. Heinonen, K. L. Wang *et al.*, Nat. Phys. **13**, 162 (2017).
[41] J. Zang, M. Mostovoy, J. H. Han, and N. Nagaosa, Phys. Rev. Lett. **107**, 136804 (2011).
[42] V. Puliafito, R. Khymyn, M. Carpentieri, B. Azzerboni, V. Tiberkevich, A. Slavin, and G. Finocchio, Phys. Rev. B **99**, 024405 (2019).
[43] K. Olejník, T. Seifert, Z. Kašpar, V. Novák, P. Wadley, R. P. Campion, M. Baumgartner, P. Gambardella, P. Nmec, J. Wunderlich *et al.*, Sci. Adv. **4**, eaar3566 (2018).
[44] P. Giannozzi, S. Baroni, N. Bonini, M. Calandra, R. Car, C. Cavazzoni, D. Ceresoli, G. L. Chiarotti, M. Cococcioni, I. Dabo *et al.*, J. Phys.: Condens. Matter **21**, 395502 (2009).
[45] A. Dal Corso, Comput. Mater. Sci. **95**, 337 (2014).
[46] J. P. Perdew, K. Burke, and M. Ernzerhof, Phys. Rev. Lett. **77**, 3865 (1996).
[47] N. Papanikolaou, R. Zeller, and P. H. Dederichs, J. Phys.: Condens. Matter **14**, 2799 (2002).
[48] D. S. G. Bauer, Ph.D. thesis, RWTH Aachen University, Germany, 2014
[49] The juKKR code can be found at https://jukkr.fz-juelich.de/.
[50] S. Vosko, L. Wilk, and M. Nusair, Can. J. Phys. **58**, 1200 (1980).
[51] H. Ebert and S. Mankovsky, Phys. Rev. B **79**, 045209 (2009).
[52] G. P. Müller, M. Hoffmann, C. Dißelkamp, D. Schürhoff, S. Mavros, M. Sallermann, N. S. Kiselev, H. Jónsson, and S. Blügel, Phys. Rev. B **99**, 224414 (2019).
[53] The Spirit code can be found at https://juspin.de.
[54] G. P. Müller, P. F. Bessarab, S. M. Vlasov, F. Lux, N. S. Kiselev, S. Blügel, V. M. Uzdin, and H. Jónsson, Phys. Rev. Lett. **121**, 197202 (2018).
[55] P. F. Bessarab, V. M. Uzdin, and H. Jónsson, Comput. Phys. Commun. **196**, 335 (2015).
[56] S. von Malottki, B. Dupé, P. F. Bessarab, A. Delin, and S. Heinze, Sci. Rep. **7**, 12299 (2017).
[57] A. S. Varentcova, S. von Malottki, M. N. Potkina, G. Kwiatkowski, S. Heinze, and P. F. Bessarab, npj Comput. Mater. **6**, 193 (2020).
[58] Y. Ou, W. Yanez, R. Xiao, M. Stanley, S. Ghosh, B. Zheng, W. Jiang, Y.-S. Huang, T. Pillsbury, A. Richardella *et al.*, Nat. Commun. **13**, 2972 (2022).
[59] S. Fragkos, P. Pappas, E. Symeonidou, Y. Panayiotatos, and A. Dimoulas, Appl. Phys. Lett. **120**, 182402 (2022).
[60] Jülich Supercomputing Centre, J. Large-Scale Res. Facilities **4**, A132 (2018).